1   **Type of paper: Original Research Paper**

2   **Title: Strain-induced trace element mobility in a quartz-sulphide vein system: An example**

3   **from the ONKALO[TM] spent nuclear fuel repository (Olkiluoto, SW Finland).**

4

5   **Marchesini B.[a]*, Menegon L.[b], Schwarz G.[c], Neff C.[c], Keresztes Schmidt P.[c], Garofalo P.S.[d],**

6   **Hattendorf B.[c], Günther D.[c], Mattila J.[e] & Viola G.[d]**

7   [a] Dipartimento di Scienze della Terra, Sapienza Università di Roma, Piazzale Aldo Moro 5, Roma,
8   Italy.
9   [b] The Njord Centre, Department of Geoscience, University of Oslo, P.O. Box 1048 Blindern,
10   Norway.
11   [c] Laboratory of Inorganic Chemistry, ETH Zürich, CH-8093 Zürich, Switzerland.
12   [d] Dipartimento di Scienze Biologiche, Geologiche ed Ambientali – BiGeA, Università di Bologna,
13   Via Zamboni 67, Bologna, Italy.
14   [e] Rock Mechanics Consulting Finland Oy, Kulloonmäentie 24 H23, 02940 Espoo, Finland.

15

16   *: corresponding author: Barbara Marchesini-barbara.marchesini@uniroma1.it.
17
18   L. Menegon – luca.menegon@geo.uio.no
19   G. Schwarz – schwarz@inorg.chem.ethz.ch
20   C. Neff – cneff@inorg.chem.ethz.ch
21   P. Keresztes Schmidt – peterke@student.ethz.ch; presently: peter.keresztes@space.unibe.ch
22   P.S. Garofalo – paolo.garofalo@unibo.it
23   B. Hattendorf – bodo@inorg.chem.ethz.ch
24   D. Günther – detlef.guenther@sl.ethz.ch
25   J. Mattila – jussi.mattila@rmcf.fi
26   G. Viola – giulio.viola3@unibo.it
27
28
29   **Keywords:** sulphides; LA-ICP-TOFMS; diffusion; chemical replacement; trace element mobility

30

31

32

33

34

35

36

Abstract

This work investigates element mobility and deformation mechanisms in sulphide-bearing quartz veins associated with a strike-slip fault exposed in the ONKALO™ Finnish deep repository for spent nuclear fuel (Olkiluoto Island, southwest Finland). It combines petrography, trace element mapping by Laser Ablation Inductively Coupled Plasma Time-of-Flight Mass Spectrometry (LA-ICP-TOFMS) and Electron Backscattered Diffraction (EBSD) analysis of representative microstructures. The fault core was repeatedly reactivated by multiple brittle deformation episodes assisted by hydrothermal fluid batches with distinct trace element signatures. LA-ICP-TOFMS element distribution maps and EBSD on sulphides reveal local, syn-deformational intragrain enrichment of primary and secondary elements (i.e., As, Co, Cu, Ag, Sn, Sb, Pb, Se, In, Te) by a combination of microscale plastic and brittle deformation at the reaction fronts. Fluid ingress along microcracks enhancing chemical alteration of pyrite combined with element diffusion along dislocations and tilt boundaries, controlled trace element mobility in sulphides at the small scale. At the scale of the vein system, the competence contrast between inclusions of soft sulphides in the harder host quartz may favor local fracture nucleation and fluid flow.

1. Introduction

Tectonic faults and fractures may behave as major fluid conduits (e.g., Caine 1996; Sibson 1996; Faulkner et al., 2010) favouring fluid flow through the Earth's crust, especially in low-permeability crystalline basements (e.g., Jamveit et al., 2018; Marchesini et al., 2019; Sibson et al. 2020; Ceccato et al., 2021). Infiltration of fluids that are in disequilibrium with the mineral assemblage of the host rock may induce precipitation of authigenic minerals as well as also enhance fluid-rock interaction by processes ranging from syn-deformational mineralogical alteration to element mobility (e.g., Molli et al., 2010; Rossetti et al. 2010; Smith et al., 2013; Williams et al., 2017; Velásquez et al., 2018). During the latter, the chemical and physical properties of the host rock may undergo significant changes (e.g., Putnis et al., 2009; Rossetti et al. 2010; Maggi et al. 2012; Fulignati et al. 2019), even affecting the

overall permeability within faulted rock volumes and, as a consequence, their overall mechanical properties (e.g., Sibson, 1975; Wintsch et al., 1995; Olsen and Scholz, 1998; Collettini et al., 2009; Cox, 2010). Faults also govern mineralization processes (e.g., Sibson, 1987; Blundell et al. 2003; Torgersen et al., 2014) in addition to having a crucial role in determining fluid transmissivity in geological reservoirs (e.g., Manzocchi et al. 2008; Agosta et al. 2009). In addition, recent studies emphasized how microscale fluid-mediated deformation of selected minerals, such as sulphides, zircon and monazite, can induce secondary element mobility (e.g., Dubosq et al., 2018; Cugerone et al., 2020; Piazolo et al. 2016; Fougerouse et al. 2021a). Studies on sulphides showed that fluid-enhanced strain localization may lead to significant secondary enrichments of trace elements and may even be responsible for concentration of economically exploitable precious metal byproducts from sulphide extraction (e.g., Au, Ge; Reddy and Hough, 2013; Dubosq et al., 2018; Cugerone et al., 2020; Fougerouse et al. 2021b). The characterization of the deformation mechanisms active in fluid-mediated brittle-ductile faults associated with quartz-sulphide veins is thus crucial to reveal the processes of deformation-induced mobility of minor and trace elements.

We studied microstructures of quartz-sulphide veins associated with a strike-slip fault system cutting through the crystalline basement exposed in the ONKALO^{TM} deep repository. The combination of sulphide imaging by Laser Ablation Inductively Coupled Plasma Time-of Flight Mass Spectrometry (LA-ICP-TOFMS) and Electron Backscattered Diffraction (EBSD) allowed us to gain a refined understanding of how intragrain structures may control trace element mobility.

We anticipate that our analysis reveal that trace element enrichments are potentially controlled by sulphide rheology and enhanced by volume-change reactions. We also observed that, at the studied conditions, some trace elements, such as Ag and Sb, are excellent tracers of intragranular deformation.

2. Geological Setting

2.1 Geological framework

The island of Olkiluoto (Fig. 1a) in southwestern Finland is made of rocks of the Paleoproterozoic Svecofennian orogenic province, which is formed by supracrustal high-grade metamorphic sequences and plutonic rocks (e.g., Kärki and Paulamäki, 2006; Fig. 1a). These rocks underwent a long history of polyphasic ductile deformation between 1.86 and 1.79 Ga that led to repeated structural overprinting and mechanical reactivation of inherited and suitably oriented shear zones under amphibolite-facies metamorphic conditions (Aaltonen et al., 2010 and 2016). During progressive regional exhumation and cooling, the Olkiluoto bedrock was affected by a long brittle deformation history starting at 1.75 Ga (Mattila and Viola, 2014). This involved both the brittle reactivation of pre-existing structures (Viola et al., 2011; Mattila and Viola, 2014; Skyttä and Torvela, 2018; Prando et al., 2020), but also the formation of new faults and joints (Marchesini et al. 2019). Marchesini et al. (2019) and Prando et al. (2020) studied in detail a system of conjugate strike-slip faults, as a representative example of late Svecofennian structures responsible of the initial embrittlement of the basement. These faults nucleated at the brittle-ductile transition and were reactivated multiple times "en route" to the surface concomitantly with the ingress of batches of overpressured hydrothermal fluids. These subvertical strike-slip fault system are oriented N-S and NW-SE, respectively. They are commonly associated with hydrothermal veins, which commonly contain sulphides (Pere et al. 2009; Marchesini et al. 2019). For one of these faults, the NW-SE-striking BFZ300, Marchesini et al. (2019) constrained the composition, temperature and pressure of the synkinematic hydrothermal fluids.

In this study we focus on rocks affected by the latest reactivation of the BFZ300 fault core. Specifically, we analyzed the chlorite-sulphide-bearing quartz veins that formed by hydrofracturing at fluid pressure conditions P_f = 140-180 MPa and temperatures between 170 and 300 °C (Stage 3 of Marchesini et al. 2019).

2.2 Fault zone architecture

The internal architecture of the BFZ300 fault was constrained by combined field structural analysis (Figs. 2a-c) and drill core logging (drill core PH21; Fig. 2d). In the following, we provide a

short description of the fault architecture and its complexities. For further details the reader is referred to Marchesini et al. (2019). The BFZ300 is a NNW-SSE-striking dextral strike-slip fault as determined by Riedel shears and dextral step-over zone (Fig. 2a). The fault cuts through amphibolite-facies migmatite, interlayered with gneiss and pegmatitic granite.

Its damage zone is defined by an increased fracture density compared to the host rock, from which it is separated by two discrete slip surfaces (Y_I planes; Fig. 2a). The damage zone contains sets of conjugate NW-SE-striking dextral and NNE-SSW-striking sinistral hybrid fractures (Fig. 2b) and laterally continuous NNW-SSE striking joints (Fig. 2b). The joints and the hybrid veins are infilled by a first generation of quartz, referred to as Qtz I. The fault core is bound by two main discrete slip surfaces (Y_{II}; Fig. 2a) oriented NNW-SSE and the core is composed by two distinct quartz veins and cataclastic layers (Fig. 2c). The older of the two quartz generations, referred to as Qtz I, contains evidence of cyclic brittle and ductile deformation. The younger generation, Qtz II, has a milky white appearance, a coarser grain size than Qtz I (>1 cm), and lacks of significant evidence of crystal-plastic deformation and recrystallization (Fig. 2c). The vein infilled by Qtz II contains small (1-2 cm) aggregates of sulphides mainly located at its center (Fig. 2d). Sulphides are present as minor phases, making-up ca. 3% of the bulk volume of the vein. Radiate chlorite is observed in textural equilibrium with Qtz II at the edge of the vein (Figs. 2d; 3a).

3. Analytical Methods

In this study, we combine petrographic documentation of fault samples with a multi-technique analytical documentation that includes elemental imaging by LA-ICP-TOFMS and determination of crystal structures and orientations by EBSD analysis. Details on accuracy, long-term reproducibility, and determination of limits of detection (LODs) of these techniques are given in the Supplementary Material file. Below, we summarize the main features that are useful for data interpretation.

3.1. Optical petrography

139 Polished thin sections of Qtz II vein were obtained from drill core PH21 (Fig. 2d). Thin sections were

140 cut orthogonal to the vein wall and parallel to the vein opening direction. The microstructural analysis

141 was conducted at the Dipartimento di Scienze Biologiche, Geologiche e Ambientali of the University

142 of Bologna with a Nikon ECLIPSE CI POL petrographic microscope via reflected- and transmitted-

143 light petrography.

144

145 3.2. Laser Ablation Inductively Coupled Plasma Time-of Flight Mass Spectrometry

146 The chemical composition of the authigenic sulphides (pyrite FeS_2; sphalerite (Zn, Fe)S; galena

147 PbS) was first determined by Electron Probe Microanalysis (EPMA) analysis (see Supplementary

148 Material).

149 The variable composition of sulphide phases determined by EPMA motivated the acquisition of

150 detailed element composition maps by LA-ICP-TOFMS to study the mass fraction and spatial

151 distribution of trace elements in the sulphide grains. We thus constructed element distribution maps of

152 a sulphide assemblage using a LA-ICP-TOFMS instrument setup developed at the Department of

153 Chemistry and Applied Biosciences, Laboratory of Inorganic Chemistry of the ETH of Zürich,

154 Switzerland. This setup uses an ICP-TOF mass spectrometer instrument (TOFWERK, Thun,

155 Switzerland) in combination with an argon fluoride (ArF) excimer LA system (193 nm, GeoLas C,

156 Lambda Physik, Goettingen, Germany) and a low-dispersion LA "tube cell" developed in-house

157 (Wang et al. 2013), which is designed for high-speed and high-resolution LA-ICPMS imaging

158 applications. While specific details of this setup are given in the Supplementary Material, we highlight

159 here that the low-dispersion LA and the ICP-TOFMS detection allows full mass spectrum acquisition

160 at high speeds.

161 The distribution maps presented here were obtained from regions of ~1 mm^2, ranging from 500x600

162 μm to 700x700 μm. These maps were generated with circular laser spot sizes 5 μm in diameter using

163 a hole-drilling approach (Neff et al.2020) a burst of 25 laser pulses per sample position. This number

164 of laser pulses leads in total to a high signal intensity per sample position (i.e., pixel), and thereby to

high pixel sensitivity and improved LODs while maintaining the lateral resolution. Elements with signal levels above their LODs at each pixel were quantified based on a 100% mass normalization procedure. The LODs ranged between hundreds of ng g^{-1} to tens of μg g^{-1} per pixel for elements across the periodic table. Across the elemental mass spectrum, 15 major, minor, and trace elements provided concentrations above LODs across a larger area to construct element distribution maps in these samples (Fe, As, Co, Cu, Sn, Sb, Zn, Ni, Pb, Cd, Ag, Mn, In, Se and Te). Only the most significant of these maps are presented and discussed here, while the others are reported in the Supplementary Material.

3.3. Electron Backscattered Diffraction

Crystallographic orientation data were obtained from automatically indexed EBSD patterns collected on a JEOL 6610 SEM at the Electron Microscopy Centre of the University of Plymouth, UK. EBSD data are presented in the form of 1) Inverse Pole Figure (IPF) maps; 2) Equal area, lower hemisphere pole figures of crystallographic orientations; 3) Local misorientation (LM) maps, 4) Texture component (TC) maps, and 5) misorientation profiles across low-angle boundaries. Further information about these maps are reported in the Supplementary Material.

4. Microstructural analysis

At the microscale, sulphide aggregates appear as complex, composite and interdigitated bodies embedded within coarse Qtz II crystals (Figs. 3a; 4a). The host quartz has a grain size between 200 μm and 5 mm (Figs. 3b-c). Close to the sulphide aggregates, the host quartz is intensely deformed by a dense network of fractures, which are marked by trails of fluid inclusions and only partially healed (Figs. 3c). Close to the sulphide aggregates the host quartz also exhibits a local distortion of the crystal lattice, as documented by undulouse extinction (Fig. 3b). A few cm away from the sulphide aggregates, the host quartz exhibits intead a lower degree of fracturing, with mostly intragranular fractures and intact growth structures, and undistorted crystals (Figs. 3d-e).

190   Sulphide aggregates are composed of pyrite, sphalerite and galena in highly variable

191   proportions. Minor chalcopyrite is locally also observed but it occurs exclusively within sphalerite in

192   the form of rows of small-sized blebs and rods (i.e., the so called "chalcopyrite disease"; Fig. S1).

193   Because of its minor occurrence, chalcopyrite is not discussed in the following LA-ICP-TOFMS maps

194   although its influence on deformation and element distribution is considered in the discussions (see

195   Section 7.4).

196   Pyrite exhibits a generally euhedral texture in equilibrium with quartz. In thin section, pyrite is seen to

197   be variably affected by late fractures that are associated with partial replacement of pristine pyrite by

198   sphalerite and galena (Figs. 4b-e). Sphalerite-galena assemblages are characterized instead by anhedral

199   textures and represent the infilling of major fractures crosscutting quartz and pyrite (Fig. 4c-e) and/or

200   the alteration overgrowths on pyrite grains (Fig. 4b). On the basis of these aforementioned

201   observations, we selected three representative portions of the studied Qtz II vein, referred to as

202   Domains 1 to 3, to document the heterogeneity in fracturing and pyrite alteration within the system

203   under consideration (Fig. 4a).

204   Pyrite in Domain 1 (marked in green in Fig. 4a) has a euhedral texture in equilibrium with quartz and

205   it is characterized by a grain size between 600 and 800 μm (Fig. 4b). The pyrite margins are corroded

206   when in contact with the sphalerite-galena assemblage (Fig. 4b). Internally, pyrite does not show

207   evidence of fracturing or replacement into sphalerite and galena. Proximal quartz is affected by

208   intragrain fractures (Fig. 4b)

209   Pyrite in Domain 2 (yellow in Fig. 4a) exhibits a subhedral texture and has a grain size between 400

210   μm and 2 mm (Fig. 4c). Dissimilar to pyrite in Domain 1, pyrite in Domain 2 is locally dissected by

211   intra- and intergranular fractures (red dashed line of Fig. 4c) and it is locally replaced by sphalerite-

212   galena assemblage. Fractures are both barren and locally sealed by sphalerite and galena (Fig. 4c).

213   Proximal quartz is affected by intra- and intergranular fractures, that are associated with sphalerite and

214   galena associations (Fig. 4c).

Pyrite in Domain 3 (red in Fig. 4a) exhibits a euhedral to subhedral habit and shows a heterogeneous grain size distribution (200-800 µm; Fig. 4d) due to the brittle fragmentation of larger crystals. Pyrite is deformed by intra- and intergranular fractures (red dashed lines of Figs. 4d-e) along which it is extensively replaced by sphalerite and galena. Sphalerite-galena assemblages seal intra- and intergranular fractures (Figs. 3d-e) as documented, albeit to a lesser extent, for pyrite in Domain 2 (Figs. 4d-e). Barren fractures in pyrite are rare (Fig. 4e). Proximal quartz is affected by intra- and intergranular fractures, which control the precipitation of sphalerite and galena (Fig. 4d).

5. LA-ICP-TOFMS element distribution maps

We analyzed the chemical composition of major, minor and trace elements within representative pyrite and sphalerite-galena assemblages from each of the three structural domains. In the following, we present in detail the distribution maps of selected elements, i.e., As, Co, Cu, Ag, Sn, Sb, Pb, Se, In and Te. These elements highlight both the primary compositional variability of sulphides and secondary enrichments. The maps of the other detected elements are available in the Supplementary Material.

5.1. Sulphides in Domain 1

In the undeformed or weakly deformed sulphides, the compositional maps highlight a direct association between minor-, trace elements enrichments and specific minerals.. The maps show in particular that pyrite is As-Co-Pb-Se-Te-Zn-Cd-bearing (Fig. 5; Fig. S2). More in detail, As and Co show enrichments at grain boundaries and internal bands sub-parallel to grain boundaries, which indicate that these elements are mostly associated with primary crystal growth (Fig. 5 b,c). Growth rims are crosscut by thin, branching "chemical structures", which mostly affect the grain (Figs. 5b-c). These intragranular chemical structures are thus marked by a local enrichment in As and Co, with mass fractions ranging between 3000 and 10.000 mg/kg (Figs. 5b-c). The observed textural relationships between growth structures and intragranular structures are sketched in Fig. 5l.

240   The trace elements Sn, Sb, Ag and Se are mostly associated with galena (with mass fractions

241   up to 100 mg/kg, Figs. 5 d-j), as inferred from the comparison with optical microstructures (Fig. 5a)

242   and Pb distribution (Fig. 5h). Se is also associated with pyrite and it occurs in mass fractions between

243   10 and 300 mg/kg (Fig. 5i). The mass fraction of Te is elevated along the pyrite-sphalerite and pyrite-

244   galena edges. Cu, In and Cd are primarily associated with sphalerite, in which they occur in mass

245   fractions as high as 10.000 mg/kg (Figs. 5d, j; S2). Also Mn is primarily associated with sphalerite but

246   it occurs at lower mass fractions (between 200 and 600 mg/kg; S2). Local enrichments of Ag, Pb and

247   Sb are visible along the intragrain structures (Figs. 5e, g, h). Irregular distributions of Co, Cu, Ag, Sb,

248   Sn and Mn in the sphalerite-galena assemblage have an internal polygonal structure (Figs. 5f-g, S2),

249   indicating sulphide precipitation during vein segregation.

250

251   *5.2. Sulphides in Domain 2*

252   Similar to what described for Domain 1, the enrichment (up to 10.000 mg/kg) of As within the

253   subhedral pyrite from Domain 2 highlights the presence of growth zoning (Figs. 6b-c). However,

254   growth rims are crosscut by several intragranular structures (Fig. 6b-k) that are marked by high mass

255   fractions (up to 1.000 mg/kg) of Co, Cu, Ag, Sn, Sb, Pb, Ni and, to a lesser extent, In, Se, and Mo

256   (Figs. 6 and S3). These structures are best outlined by the distributions of Sb, Ag, Sn and show

257   irregular branching shapes with variable orientations in the pyrite grain (Figs. 6d-h). The textural

258   relationships between grow structures and the network of structures in Domain 2 are schematized in

259   Fig. 6l. A macroscopic open fracture in the right-hand side of the scanned area (Fig. 6a) shows edges

260   enriched with trace elements associated with sphalerite and galena.

261   Cu, In and Te are mostly associated with sphalerite (Figs. 6d, j, k). High Se mass fractions are found

262   in galena (> 1000 mg/kg) although it also occurs in pyrite with mass fraction between 10 and 300

263   mg/kg (Fig. 6i), as in Domain 1.

264

265   *5.3. Sulphides in Domain 3*

266   Pyrite in Domain 3 contains As and Co a mass fractions of <10.000 mg/kg and systematically

267   lower values of all other trace elements (Figs. 7, S4). The sphalerite-galena assemblage contains the

268   same minor and trace elements that we documented in Domain 2 (i.e., Cu, Ag, Sn, Sb, Se, In, Te, Ni,

269   Cd, Mn), with mass fraction values ranging between 1.000 and 100 mg/kg (Figs. 7, S4).

270   Primary growth structures in pyrite are only faintly outlined by the elemental distribution of As and

271   Co (Figs. 7b-c). Growth rims are very discontinuous and they are only locally visible (Figs. 7b-c).

272   Pyrite aggregates are crosscut by a pervasive network of intra- and intergranular structures, which are

273   marked by high mass fractions of the above-mentioned trace elements (Fig. 7). Some of these

274   structures are also decorated by galena and sphalerite (Fig 7h). The textural relationships between

275   growth structures and the observed network of structures are conceptualized in Fig. 7l.

276   As for Domain 2, Sb, Ag and Sn best define the intragranular microstructure. Sb in particular, not only

277   highlights the same fracture network as Ag and Sn, but it also shows a spatial correlation with

278   enrichment structures of Co.

279   Cu and In are mostly associated with sphalerite, whereas Te and Se are mostly associated with galena

280   (as in Domain 1). As noted above, Se is also associated with pyrite and it occurs in mass fractions

281   between 10 and 300 mg/kg (Fig. 7i)

282

283   **6. EBSD analysis of pyrite**

284   LA-ICP-TOFMS imaging of pyrite grains documents the presence of several chemical features

285   that could not be revealed by standard petrographic analysis. We used electron back-scattered

286   diffraction (EBSD) to verify the nature of intragranular features identified in the trace elements maps.

287   They can in fact correspond to both lattice distortions or, in general, to misorientation bands or

288   microcracks that could have represented pathways for intragranular element mobility.

289   Because of the destructive nature of the LA-ICP-TOFMS mass spectrometry, EBSD maps could not

290   be acquired on exactly the same areas mapped by LA-ICP-TOFMS. EBSD analysis had therefore to

291   be done on areas located as close as possible to those investigated chemically, but still within the same

292   grain (Figs. 8a,9a). Pyrite in Domain 1 could not be analyzed by EBSD.

293   On all EBSD maps and pole figures, the X direction is the pole to the vein wall (Figs. 8b, 9b).

294

295   *6.1. EBSD maps of Domain 2*

296   The inverse pole figure (IPF) coloring scheme of the pyrite grains within Domain 2 shows the

297   presence of three pyrite grains (Fig. 8b) wherein several low-angle boundaries are identified

298   (highlighted by white lines in Fig. 8b), corresponding to misorientation values between 1.5 and 10°.

299   Grain 1 and grain 2 in Fig. 8b display low-angle boundaries oriented at 45°-50° from the base of the

300   map. Another low-angle boundary is present within grain 3; it is oriented at 10°-15° from the base of

301   the map (Fig. 8b) and it exhibits a sutured geometry.

302   The local misorientation map (LM; see Supplementary Material for method) shows that pyrite grains

303   contain several substructures characterized by local misorientations of up to 2.5° (Fig. 8c), the most

304   prominent of which are the identified low-angle boundaries. The texture component map (TC; see

305   Supplementary material) of Grain 1 highlights up to 4° of intracrystalline distortion, which is

306   accommodated across misorientation bands and low angle boundaries oriented at 45-70° from the base

307   of the map (Figs. 8d, e).

308   The TC map of grain 3 shows a more complex and variable misorientation distribution, where the

309   maximum misorientation is about 4-4.5° and is mainly found along the pyrite grain outer edges (Fig.

310   8f). The misorientation profile across the low-angle boundary within grain 3 with a sutured geometry

311   (segment c-d, Fig. 8f) shows that the cumulative lattice misorientation is on average c. 3° with a sharp

312   misorientation step in the profile across the low-angle boundary located at c. 60 μm from point "c"

313   (Fig. 8g).

314   To integrate the results from the cumulative misorientation profile collected from grain 1, pole figures

315   are plotted for a subset sampled across the low-angle boundary within grain 1 (Fig. 8h). The location

316   of the sampled area is highlighted by a dashed white rectangle in Fig. 8d. The boundary trace analysis

of the low-angle boundary provides a solution for the most feasible slip plane and slip direction relative to the rotation axes (Fig. 8h), assuming a tilt boundary geometry. The dispersion paths on the pole figures identify <100> as the rotation axis. A tilt boundary plane containing the boundary trace of the low-angle boundary and the rotation axis is consistent with these data (Fig. 8h).

6.2. EBSD maps of Domain 3

The inverse pole figure coloring scheme of the pyrite grain mapped within Domain 3 shows the existence of a few low-angle boundaries (highlighted by white lines in Fig. 9b) with orientation spanning from 10-15° from the base of the map (named "I", Fig. 9b) to c. 140° (named "II", Fig. 9b). The LM map shows that the grain contains a network of substructures characterized by local misorientation of up to 1.5°, of which the low-angle boundaries shown in Fig. 9b are the most prominent (Fig. 9c). The TC map shows that the lattice distortion is accumulated across the identified low-angle boundaries (Fig. 9d). The misorientation profile across low-angle boundary "I" (a-b, Fig. 9d) shows a progressive lattice distortion along the first half of the profile, followed by a sharp misorientation of ca. 1.5° in correspondence of the low-angle boundary itself. In the second half of the profile, the misorientation accumulated is relatively low (<1°), indicating that the two portions of the grain sampled by the profile have a different extent of internal lattice distortion (Fig. 9e). A second misorientation profile is acquired across low-angle boundary "II" (c-d, Fig. 9d). Here, the cumulative lattice misorientation reaches a maximum value of 7.5° (Fig. 9f) and is accommodated by a sharp misorientation increase across the two low-angle boundaries sampled by the profile (Fig. 9f). Pole figures are plotted for a subset sampled across low-angle boundary "I" (Fig. 9g; the sampled area is delimited by a white dashed rectangle in Fig. 9d). The dispersion paths on the pole figures identify <100> as the rotation axis (Fig. 9g). A tilt boundary plane containing the boundary trace of the low-angle boundary and the rotation axis is consistent with these data (Fig. 9g).

7. Discussion

7.1. Sulphide composition and trace element distribution

LA-ICP-TOFMS maps show that the distribution of trace elements enrichments in sulphides (i.e., Co, Cu, Ag, Sn, Sn, Pb, Se, In, Te) correspond to a network of intragranular structures, which are referred to as "chemical structures". Trace and minor element variability in crystal lattices of sulphides is extensively documented in literature (e.g., Fleet et al., 1993; Abraitis et al., 2004; Blanchard et al, 2007; Vukmanovic et al. 2014; Sykora et al., 2018). As and Co are common pyrite components, as they are incorporated into its crystal structure at mass fractions as high as 10 wt% (e.g., Abraitis et al., 2004; Blanchard et al, 2007; Sykora et al., 2018). Hence, their occurrence as the most abundant trace elements in pyrite, at mass fractions that reach about 1 wt% and 0.1 wt%, respectively, is expected. Considerations similar to those made for pyrite can be made for the occurrence of Cu, In, Cd and Mn within sphalerite (Figs. 5-7; Figs. S1-S3). These trace elements are reported in the literature among the most typical for sphalerite, and their mass fractions can be as high as 6-7 wt% (e.g., sphalerite is the main ore mineral for Cd; Cook et al., 2009). The abundance of these elements in the studied sphalerite ranges between c. 0.03 wt% (for In) and 1 wt% (Cd and Cu), and is therefore close to the average values documented in natural samples. Similarly, galena from several geological environments shows Ag, Sb, Sn, and Se with proportions varying from few tens of ppm to 1.5 wt% (e.g., George et al, 2015; Palero-Fernandez and Martin-Izard, 2005). The values of these trace elements in the analyzed galena correspond to the lower values of this range (i.e., Ag: 0.02-0.03 wt%; Sb: c. 0.001 wt%; Sn: c. 0.1 wt%). On the contrary, Se in galena is measured at mass fractions that exceed 1 wt% in our samples (Figs. 5-7).. The mass fraction of Se in the analyzed galena is close to the highest Se value documented so far in galena from several ore deposits (i.e., c. 1.8 wt%. George et al, 2015).

Our LA-ICP-TOFMS maps reveal how the inclusion of many of these known traces in sulphides occur during crystallization (e.g., As and Co) or during deformation. In particular, they reveal which elements (Ag, Sb) are good tracers of intragranular deformation processes in this geological environment.

368 As and Co are included in pyrite from its crystallization, as suggested by their involvement in primary

369 growth rims (Figs. 5-6). Growth bands in pyrite highlighted by As and Co have been documented in

370 several environments (e.g., Fleet et al., 1993). Incorporation of As into the pyrite structure takes place

371 at the expenses of S, while incorporation of Co takes place at the expenses of mainly Fe (i.e.

372 stoichiometric substitutions). However, Co is also associated with sphalerite and galena deformation

373 structures (Figs. 5-7). Although the distributions of As and Co are mainly along growth rims, element

374 distribution maps show that they are locally enriched also along network of intragranular structures

375 (Figs. 5l, 6l, 7l). On the contrary, distribution maps of Cu, Ag, Sn, Sb, Pb, Se, In, Te show that these

376 elements are predominantly associated with sphalerite-galena assemblages (Figs. 5-7). In pyrite these

377 elements are revealed by intragranular structures.

378

379 *7.2. Deformation mechanisms in pyrite*

380 In addition to the fractures that are directly visible by traditional optical microscopy, EBSD mapping

381 documents the presence of several low-angle boundaries in the pyrite grains, which we discuss further

382 below. Tilt boundary formation in pyrite is consistent with the misorientation profiles (Fig. 8e and 9e)

383 and with the boundary trace analysis (Figs. 8h, 9g) of low-angle boundaries identified in Domains 2

384 and 3. Boundary trace analysis indicates that rotation occurred along a single <100> axis. As the (100),

385 (010) and (001) planes in the cubic crystal system are symmetrically equivalent, which means that the

386 pole figures are identical, tilt boundaries can be explained by the activity of the {001}<100> slip

387 system. This inference is compatible with early work on naturally deformed pyrite from Van Goethem

388 et al. (1987) that indicates the {001}<100> slip system as the primary slip system in pyrite. Later

389 experimental work on pyrite (e.g. Cox, 1981; Barrie et al., 2008) confirmed that the {001}<100> is

390 the slip system most easily activated between 600 and 700°C. Here, however, we show that this slip

391 system may be activated also at a much lower temperature, that is, < 300 °C, as estimated in Marchesini

392 et al. (2019).

Microcracking of pyrite, possibly leading to enhanced trace element mobility (see section 7.4) is also revealed by EBSD. The cumulative misorientation profiles collected across some subgrain boundaries (e.g., Figs. 8g and 9f) show abrupt misorientation jumps of up to 3°. This abrupt misorientation of the crystalline lattice can be interpreted as due to the effect of incipient microcracking. These effects can be discriminated from those reflecting lattice distortion and tilt boundary formation as the latter are more gradual and continuous in space, such as, for example, the case shown in Figures 8e, 9e or close to the abrupt change in misorientation in Fig. 9f.

To conclude, texture component maps of single grains, misorientation profiles across low-angle boundaries and boundary trace analysis of portions of low-angle boundaries suggest that intragranular deformation in the studied system was accommodated by a combination of low-T plasticity and microfracturing. The transition from brittle to crystal-plastic behavior of pyrite was estimated in the ~200 °C to 450 °C temperature range (Graf et al. 1981; Barrie et al.; 2009; Barrie et al. 2011). Geothermometric constraints by Marchesini et al. (2019) indicate that the studied Qtz II vein precipitated and was subsequently deformed between 170 and 300 °C. These conditions are, therefore, consistent with our observations of competing, yet coexisting, crystal plastic and brittle deformation mechanisms.

7.3. Strain-induced trace element mobility

The coexisting brittle and plastic intragranular structures suggest that the observed trace element enrichments may be related to deformation processes. Trace elements may have been fluid transported and distributed by fluid percolation with associated mineral-fluid reactions along microcracks. Alternatively, they may have been concentrated within crystals by the activity of high-diffusivity pathways, such as tilt boundaries or dislocations. Boudier et al. (2010) suggested that fluids can preferentially ingress the lattice of mineral phases along dislocation walls. Also, several studies have already documented that intracrystalline deformation may induce differential element mobility, which, in turn, results in abrupt changes of element concentrations (e.g., Reddy and Hough, 2013; Piazolo et

16

al., 2016; Cugerone et al., 2020; Peterman et al., 2016; Fougerouse et al., 2019; Dubosq et al., 2019; Ribeiro et al., 2020).

Segregation of trace elements from the crystalline lattice and local accumulation along single dislocations or dislocation arrays may occur by means of mechanisms such as pipe diffusion (Love, 1964) and /or dislocation impurity pair diffusion (DIP diffusion; Petukhov and Klyuchnik, 2012) mechanisms. In the pipe diffusion model dislocation arrays act as "pipes" along which slow-diffusing components, such as heavy trace elements, are able to preferentially migrate (Vukmanovic et al., 2014). This process thus requires a chemical potential gradient between the grain and an external phase, possibly an intergranular fluid phase (Vukmanovic et al., 2014), and is commonly associated with dislocation arrays (Love, 1964), although it has been shown that it can also be efficient along single dislocations (Legros et al., 2008). The aforementioned gradient can result from the presence of chemical or structural sinks, such as precipitates and chemically enriched or depleted volumes of the crystal (Legros et al., 2008; Piazolo et al., 2016) or the core-to-core overlap of entangled dislocations or microfractures (Dubosq et al., 2019). In the DIP diffusion model, solute atoms close to dislocations are initially captured by the strain field created by the moving dislocations (Cottrell atmosphere; Cottrell and Bilby 1949) and concentrated along the dislocation itself. This causes a preferential remobilization of elements by the moving dislocations and their enrichment along the dislocations themselves (Cottrell and Bilby, 1949; Vukmanovic et al., 2014; Piazolo et al., 2016; Fougerouse et al., 2019).

Dubosq et al. (2019) suggested that pipe and DIP diffusion processes may be simultaneously active in pyrite at temperatures typical of greenschist facies conditions (260-450 °C). Conversely, we have documented that, in pyrite, these mechanisms may activate element mobility even at temperatures as low as 170-300 °C. In addition, pipe and DIP diffusion could have combined with microcrack propagation induced by stress concentration at the reaction fronts. The combined effect of these mechanisms may have contributed to mobilize a far greater range of trace elements in sulphides than

17

444 documented in previous studies (Reddy and Hough, 2013; Dubosq et al., 2019; Fougerouse et al., 2019;

445 George et al., 2018).

446

447 *7.4. Fracturing and pyrite replacement in the BFZ300 fault system*

448 The microstructural analysis of the sulphide-bearing quartz vein shows that quartz is texturally

449 in equilibrium with radiate chlorite (Fig. 3a). Additionally, also quartz and pyrite exhibit equilibrium

450 textures (Fig. 4). We interpret this evidence as supporting the primary cogenetic character of pyrite

451 and quartz-chlorite (Fig. 10a), which precipitated from a first batch of fluids rich in As and Co (Figs.

452 5-7). Conversely, sphalerite-galena-chalcopyrite assemblages are mainly found along fractures and as

453 pyrite replacement (Figs. 4c-e), suggesting that they crystallized at a later stage from a renewed ingress

454 of hydrothermal fluids, possibly enriched in Co, Cu, Ag, Sn, Sb, Pb, Se, In and Te (Figs. 5-7; Fig. 10a).

455 Given the relative mechanical weakness of pyrite with respect to quartz (e.g., Aguilar-Santillan, 2008;

456 Evans, 1984), it is possible that the presence of pyrite inclusions embedded in quartz host may

457 potentially have enhanced local fracturing by stress concentration phenomena. This, in turn, may have

458 favored the later percolation of the fluid batch that caused the sph-gal-ccp precipitation (Fig. 10a).

459 At the grain scale, replacement of pyrite by the new fluid batch was enhanced by the brittle and

460 plastic deformation mechanisms discussed above (Section 8.3). Within microfractures, the

461 precipitation of new mineral phases may have promoted fracture propagation and further alteration by

462 volume expansion reactions at the crack tips (Fig. 10b). Volume expansion reactions have been

463 documented in a number of geological settings including retrograde metamorphism during exhumation

464 of metamorphic rocks (Jamtveit et al. 2008; van der Straaten et al. 2008; Okamoto et al. 2015),

465 peridotite serpentinization (Iyer et al. 2008; Plümper et al. 2012), hydrothermal mineralization (Zhao

466 et al. 2014; Li et al. 2015; Ulven et al. 2017; Zhang et al. 2020).

467 In our system, sphalerite, galena and chalcopyrite have a larger molar volumes than the host pyrite, at

468 least at room temperature (e.g., Robie and Bethke 1962). A volume-expansion reaction of these

469 minerals may have exploited microfractures and the (110) and (100) cleavages of pyrite. For

18

470 chalcopyrite replacement, the process of reaction-induced expansion has been experimentally

471 documented by Zhang et al. (2020) at T ~200 °C. Considering large volume expansion coefficients

472 (Fei, 1995), the same process of reaction-induced deformation can be inferred also for galena and

473 sphalerite. These deformations are portrayed by trace element distribution, and in particular by Ag and

474 Sb in the structural domains with the highest degree of fracturing and replacement of pyrite (Domains

475 2-3; Figs. 6-7).

476

477 **8. Conclusions**

478 This study investigates the trace element content in a sulphide-bearing quartz vein associated

479 with a strike-slip fault system by combining microstructural analysis and high-spatial resolution

480 mapping of trace elements in fault rocks. The obtained LA-ICP-TOFMS dataset shows that trace

481 elements are enriched along several intragranular "chemical features". EBSD analysis shows that these

482 enrichments may be related to microcracks and tilt boundaries. At the reaction fronts, trace element

483 mobility and chemical replacement is promoted by diffusion along tilt boundaries and dislocations and

484 may be promoted by reactions inducing net volume changes. Precipitation of new mineral phases

485 within fractures enhances the alteration of pristine minerals and microfracture propagation.

486 We observed that in the case of deformed sulphides, the distributions of As and Co in pyrite can be

487 used as a marker to study primary growth structures. Conversely, Sb, Ag and Sn are the most effective

488 tracers of intragranular deformation at the studied conditions. This suggests that, in deformed sulphide

489 aggregates at the studied conditions, these elements migrate more easily than the other tracers.

490 To conclude, this study highlights the importance of coupling microscale structural analysis

491 with high-spatial resolution trace element mapping of fault rocks to investigate strain-induced element

492 mobility within chemically reactive fault zones.

493

494 **Author contributions**

19

BM, GV and LM, conceived the paper. BM collected and processed laboratory data, provided their interpretations, drew the figures and wrote the paper. JM and GV sampled the outcrop and contributed to the interpretation of field data. BM, GS, CN, PKS, PSG, BH and DG acquired, processed and interpreted the LA-ICP-TOFMS data. BM and LM acquired and processed the EBSD maps. All author actively participated in discussing the results and drawing the conclusions.

References

Aaltonen, I., Lahti, M., Engström, J., Mattila, J., Paananen, M., Paulamäki, S., Gehör, S., Kärki, A., Ahokas, T., Torvela, T. and Front, K., 2010. Geological model of the Olkiluoto site, Version 2.0, Posiva Working Report 2010- 70, Posiva Oy, Eurajoki.

Aaltonen, I., Engström, J., Front, K., Gehör, S., Kosunen, P. and Kärki, A., 2016. Geology of Olkiluoto. Posiva Working Report 2016- 16., Posiva Oy, Eurajoki.

Abraitis, P. K., Pattrick, R. A. D., & Vaughan, D. J., 2004. Variations in the compositional, textural and electrical properties of natural pyrite: a review. International Journal of Mineral Processing, 74(1-4), 41-59.

Agosta, F., Alessandroni, M., Tondi, E., & Aydin, A. (2009). Oblique normal faulting along the northern edge of the Majella Anticline, central Italy: Inferences on hydrocarbon migration and accumulation. Journal of Structural Geology, 31(7), 674-690.

Aguilar-Santillan, J. 2008. Elastic and hardness anisotropy and the indentation size effect of pyrite (FeS2) single

525   crystal. Acta materialia, 56(11), 2476-2487.

526   Barrie, C. D., Boyle, A. P. & Prior, D. J., 2007. An analysis of the microstructures developed in experimentally
527   deformed polycrystalline pyrite and minor sulphide phases using electron backscatter diffraction. Journal of
528   Structural Geology, 29, 1494-1511.

529   Barrie, C. D., Boyle, A. P., & Salter, M., 2009. How low can you go?-Extending downwards the limits of plastic
530   deformation in pyrite. Mineralogical Magazine, 73(6), 895-913.

531   Barrie, C. D., Pearce, M. A., & Boyle, A. P., 2011. Reconstructing the pyrite deformation mechanism map. Ore
532   Geology Reviews, 39(4), 265-276.

533   Barton, P. B., & Bethke, P. M., 1987. Chalcopyrite disease in sphalerite; pathology and epidemiology. American
534   Mineralogist, 72(5-6), 451-467.

535   Blanchard, M., Alfredsson, M., Brodholt, J., Wright, K., & Catlow, C. R. A., 2007. Arsenic incorporation into
536   FeS_2 pyrite and its influence on dissolution: a DFT study. Geochimica et Cosmochimica Acta, 71(3), 624-630.

537   Blundell, D. J., Karnkowski, P. H., Alderton, D. H. M., Oszczepalski, S., & Kucha, H., 2003. Copper
538   mineralization of the Polish Kupferschiefer: a proposed basement fault-fracture system of fluid flow. Economic
539   Geology, 98(7), 1487-1495.

540   Boudier, F., Baronnet, A., & Mainprice, D., 2010. Serpentine mineral replacements of natural olivine and their
541   seismic implications: Oceanic lizardite versus subduction-related antigorite. Journal of Petrology, 51(1-2), 495-
542   512.

543   Caine, J. S., Evans, J. P. and Forster, C. B., 1996. Fault zone architechture and permeability structure, Geology,
544   24(11), 1025–1028, doi:10.1130/0091-7613(1996)024<1025.

545   Ceccato, A., Viola, G., Tartaglia, G., & Antonellini, M., 2021. In–situ quantification of mechanical and
546   permeability properties on outcrop analogues of offshore fractured and weathered crystalline basement:
547   Examples from the Rolvsnes granodiorite, Bømlo, Norway. Marine and Petroleum Geology, 124, 104859.

548   Collettini, C., Niemeijer, A., Viti, C., & Marone, C., 2009. Fault zone fabric and fault
549   weakness. Nature, 462(7275), 907-910.

550   Cook, N. J., Ciobanu, C. L., Pring, A., Skinner, W., Shimizu, M., Danyushevsky, L., Saini-Eidukat, B., &
551   Melcher, F., 2009. Trace and minor elements in sphalerite: A LA-ICPMS study. Geochimica et Cosmochimica
552   Acta, 73(16), 4761-4791.

553   Cottrell, A. H., & Bilby, B. A., 1949. Dislocation theory of yielding and strain ageing of iron. Proceedings of
554   the Physical Society. Section A, 62(1), 49.

555   Cox, S. F., 2010. The application of failure mode diagrams for exploring the roles of fluid pressure and stress
556   states in controlling styles of fracture-controlled permeability enhancement in faults and shear
557   zones. Geofluids, 10(1-2), 217-233.

558   Cox, S. F., Etheridge, M. A., & Hobbs, B. E., 1981. The experimental ductile deformation of polycrystalline
559   and single crystal pyrite. Economic Geology, 76(8), 2105-2117.

560   Cugerone, A., Cenki-Tok, B., Oliot, E., Muñoz, M., Barou, F., Motto-Ros, V., & Le Goff, E., 2020.
561   Redistribution of germanium during dynamic recrystallization of sphalerite. Geology, 48(3), 236-241.

562   Dubosq, R., Lawley, C. J. M., Rogowitz, A., Schneider, D. A., & Jackson, S., 2018. Pyrite deformation and
563   connections to gold mobility: Insight from micro-structural analysis and trace element mapping. Lithos, 310,
564   86-104.

565 Dubosq, R., Rogowitz, A., Schweinar, K., Gault, B., & Schneider, D. A., 2019. A 2D and 3D nanostructural
566 study of naturally deformed pyrite: assessing the links between trace element mobility and defect
567 structures. Contributions to Mineralogy and Petrology, 174(9), 72.

568 Evans, B. (1984). The effect of temperature and impurity content on indentation hardness of quartz. Journal of
569 Geophysical Research: Solid Earth, 89(B6), 4213-4222.

570 Faulkner, D. R., Jackson, C. A. L., Lunn, R. J., Schlische, R. W., Shipton, Z. K., Wibberley, C. A. J., & Withjack,
571 M. O., 2010. A review of recent developments concerning the structure, mechanics and fluid flow properties of
572 fault zones. Journal of Structural Geology, 32(11), 1557-1575.

573 Fei, Y., 1995. Thermal expansion, in: Mineral physics and crystallography: a handbook of physical
574 constants, Ahrens, T. J., 2, 29-44.

575 Fleet, M. E., Chryssoulis, S. L., MacLean, P. J., Davidson, R., & Weisener, C. G., 1993. Arsenian pyrite from
576 gold deposits; Au and As distribution investigated by SIMS and EMP, and color staining and surface oxidation
577 by XPS and LIMS. The Canadian Mineralogist, 31(1), 1-17.

578 Fougerouse, D., Reddy, S. M., Seydoux-Guillaume, A. M., Kirkland, C. L., Erickson, T. M., Saxey, D. W.,
579 Rickard, W.D.A., Jacob, D., Leroux, H. & Clark, C., 2021a. Mechanical twinning of monazite expels
580 radiogenic lead. Geology, 49(4), 417-421.
581
582 Fougerouse, D., Reddy, S. M., Aylmore, M., Yang, L., Guagliardo, P., Saxey, D.W., William D.A. Rickard, W.
583 D.A. and Timms, N., 2021b. A new kind of invisible gold in pyrite hosted in deformation-related dislocations.
584 Geology, Volume XX, Number XX.

585 Fougerouse, D., Reddy, S. M., Kirkland, C. L., Saxey, D. W., Rickard, W. D., & Hough, R. M., 2019. Time-
586 resolved, defect-hosted, trace element mobility in deformed Witwatersrand pyrite. Geoscience Frontiers, 10(1),
587 55-63.

588 Fulignati, P., Agosta, F., Belviso, C., Prosser, G., Lettino, A., Petrullo, A. V., & Cavalcante, F. (2019). Structural
589 and Mineralogical Characterization of a Fossil Hydrothermal System Located at the Outermost Front of the
590 Southern Apennines Fold-and-Thrust Belt. Geofluids, 2019.

591 George, L., Cook, N. J., Ciobanu, C. L., & Wade, B. P., 2015. Trace and minor elements in galena: A
592 reconnaissance LA-ICP-MS study. American Mineralogist, 100(2-3), 548-569.

593 George, L., Biagioni, C., D'Orazio, M., & Cook, N. J., 2018. Textural and trace element evolution of pyrite
594 during greenschist facies metamorphic recrystallization in the southern Apuan Alps (Tuscany, Italy): influence
595 on the formation of Tl-rich sulfosalt melt. Ore Geology Reviews, 102, 59-105.

596 Graf, J. L., Skinner, B. J., Bras, J., Fagot, M., Levade, C., & Couderc, J. J., 1981. Transmission electron
597 microscopic observation of plastic deformation in experimentally deformed pyrite. Economic Geology, 76(3),
598 738-742.
599
600 Iyer,K., Jamtveit,B., Mathiesen,J., Malthe-Sørenssen,A. & Feder, J., 2008. Reaction assisted hierarchical
601 fracturing during serpentinization. Earth Planet. Sci. Lett. 267, 503–516.

602 Jamtveit, B., Malthe-Sørenssen, A. & Kostenko, O., 2008. Reaction enhanced permeability during retrogressive
603 metamorphism. Earth Planet. Sci. Lett. 267, 620–627.

604 Kärki, A., & Paulamäki, S., 2006. Petrology of Olkiluoto (No. POSIVA--06-02). Posiva Oy.

605 Legros, M., Dehm, G., Arzt, E., & Balk, T. J., 2008. Observation of giant diffusivity along dislocation
606 cores. Science, 319(5870), 1646-1649.

607 Li, K. Pring, A., Etschmann, B., Macmillan, E., Ngothai, Y., O'Neill, B., Hooker, A., Mosselmans, F. &

608   Brugger, J., 2015. Uranium scaveng- ing during mineral replacement reactions. Am. Mineral. 100, 1728–1735.

609   Love, G. R., 1964. Dislocation pipe diffusion. Acta Metallurgica, 12(6), 731-737.

610   Maggi, M., Rossetti, F., Corfu, F., Theye, T., Andersen, T. B., & Faccenna, C. (2012). Clinopyroxene–rutile
611   phyllonites from the East Tenda Shear Zone (Alpine Corsica, France): pressure–temperature–time constraints
612   to the Alpine reworking of Variscan Corsica. Journal of the Geological Society, 169(6), 723-732.

613   Manzocchi, T., Heath, A. E., Palananthakumar, B., Childs, C., & Walsh, J., 2008. Faults in conventional flow
614   simulation models: a consideration of representational assumptions and geological uncertainties. Petroleum
615   Geoscience, 14(1), 91-110.

616   Marchesini, B., Garofalo, P. S., Menegon, L., Mattila, J., & Viola, G., 2019. Fluid-mediated, brittle–ductile
617   deformation at seismogenic depth–Part 1: Fluid record and deformation history of fault veins in a nuclear waste
618   repository (Olkiluoto Island, Finland). Solid Earth, 10(3), 809-838.

619   Mattila, J. and Viola, G., 2014. New constraints on 1.7 Gyr of brittle tectonic evolution in southwestern Finland
620   derived from a structural study at the site of a potential nuclear waste repository (Olkiluoto Island), J. Struct.
621   Geol., 67(PA), 50–74, doi:10.1016/j.jsg.2014.07.003.

622   Molli, G., Cortecci, G., Vaselli, L., Ottria, G., Cortopassi, A., Dinelli, E. & Barbieri, M., 2010. Fault zone
623   structure and fluid–rock interaction of a high angle normal fault in Carrara marble (NW Tuscany, Italy). Journal
624   of Structural Geology, 32(9), 1334-1348.

625   Neff, C., Schmidt, P. K., Garofalo, P. S., Schwarz, G., & Günther, D., 2020. Capabilities of automated LA-ICP-
626   TOFMS imaging of geological samples. Journal of Analytical Atomic Spectrometry, 35(10), 2255-2266.

627   Olsen, M. P., Scholz, C. H., & Léger, A., 1998. Healing and sealing of a simulated fault gouge under
628   hydrothermal conditions: Implications for fault healing. Journal of Geophysical Research: Solid Earth, 103(B4),
629   7421-7430.

630   Okamoto, A. & Shimizu, H., 2015. Contrasting fracture patterns induced by volume-increasing and-decreasing
631   reactions: Implications for the progress of metamorphic reactions. Earth Planet. Sci. Lett. 417, 9–18.

632   Palero-Fernández, F. J., & Martín-Izard, A., 2005. Trace element contents in galena and sphalerite from ore
633   deposits of the Alcudia Valley mineral field (Eastern Sierra Morena, Spain). Journal of Geochemical
634   Exploration, 86(1), 1-25.

635   Pere, T., 2009. Fault-related Local Phenomena in the Bedrock of Olkiluoto, with Particular Reference to Fault
636   Zone OL-bfz100. Working Report 2009-125, Posiva Oy, Eurajoki. pp. 98.

637   Peterman, E. M., Reddy, S. M., Saxey, D. W., Snoeyenbos, D. R., Rickard, W. D., Fougerouse, D., & Kylander-
638   Clark, A. R., 2016. Nanogeochronology of discordant zircon measured by atom probe microscopy of Pb-
639   enriched dislocation loops. Science Advances, 2(9), e1601318.

640   Petukhov, B. V., & Klyuchnik, P. A., 2012. Dynamic interaction of dislocations with impurity subsystem in
641   crystalline materials. Crystallography Reports, 57(3), 388-392.

642   Piazolo, S., La Fontaine, A., Trimby, P., Harley, S., Yang, L., Armstrong, R., & Cairney, J. M., 2016.
643   Deformation-induced trace element redistribution in zircon revealed using atom probe tomography. Nature
644   communications, 7, 10490.

645   Plümper,O., Røyne,A., Magrasó,A. & Jamtveit,B., 2012. Theinterface-scalemechanismofreaction-
646   inducedfracturingduringserpen- tinization. Geology 40, 1103–1106.

647   Prando F., Menegon L., Anderson M. W., Marchesini B., Mattila J. and Viola, G., 2020. Fluid-mediated, brittle-
648   ductile deformation at seismogenic depth: Part II – Stress history and fluid pressure variations in a shear zone

23

649   in a nuclear waste repository (Olkiluoto Island, Finland). Solid Earth, 11, 489–511,
650   https://doi.org/10.5194/se-11-489-2020.

652   Putnis, A., 2009. Mineral replacement reactions. Reviews in mineralogy and geochemistry, 70(1), 87-124.

654   Ribeiro, B. V., Lagoeiro, L., Faleiros, F.M., Hunter, N.J.R., Queiroga, G., Raveggi, M., Cawood, P.A., Finch,
655   M., & Campanha, G.A.C, 2020. Strain localization and fluid-assisted deformation in apatite and its influence
656   on trace elements and U–Pb systematics. Earth and Planetary Science Letters 545 11642.

658   Reddy, S. M., & Hough, R. M., 2013. Microstructural evolution and trace element mobility in Witwatersrand
659   pyrite. Contributions to Mineralogy and Petrology, 166(5), 1269-1284.

661   Robie, R. A., & Bethke, P. M., 1962. Molar volumes and densities of minerals. Unites States Department of the
662   Interior Geological Survey, 4-21.

664   Rossetti, F., Aldega, L., Tecce, F., Balsamo, F., Billi, A., & Brilli, M., 2011. Fluid flow within the damage zone
665   of the Boccheggiano extensional fault (Larderello–Travale geothermal field, central Italy): structures, alteration
666   and implications for hydrothermal mineralization in extensional settings. Geological Magazine, 148(4), 558-
667   579.

669   Sibson, R. H., Moore, J. M. M., & Rankin, A. H., 1975. Seismic pumping—a hydrothermal fluid transport
670   mechanism. Journal of the Geological Society, 131(6), 653-659.

672   Sibson, R. H., 1987. Earthquake rupturing as a mineralizing agent in hydrothermal systems. Geology, 15(8),
673   701-704.

675   Sibson, R. H., 1996. Structural permeability of fluid-driven fault-fracture meshes, J. Struct. Geol, 18(8).

677   Sibson, R. H., 2020. Preparation zones for large crustal earthquakes consequent on fault-valve action. Earth,
678   Planets and Space, 72(1), 1-20.

680   Skyttä, P. and Torvela, T., 2018. Brittle reactivation of ductile precursor structures: The role of incomplete
681   structural transposition at a nuclear waste disposal site, Olkiluoto, Finland, J. Struct. Geol., 0–1,
682   doi:10.1016/j.jsg.2018.06.009.

683   Smith, S. A., Bistacchi, A., Mitchell, T. M., Mittempergher, S., & Di Toro, G., 2013. The structure of an
684   exhumed intraplate seismogenic fault in crystalline basement. Tectonophysics, 599, 29-44.

685   Sykora, S., Cooke, D. R., Meffre, S., Stephanov, A. S., Gardner, K., Scott, R., Selley, D., & Harris, A. C.,
686   2018. Evolution of pyrite trace element compositions from porphyry-style and epithermal conditions at the
687   Lihir gold deposit: Implications for ore genesis and mineral processing. Economic Geology, 113(1), 193-208.

689   Torgersen, E., & Viola, G., 2014. Structural and temporal evolution of a reactivated brittle–ductile fault–Part I:
690   Fault architecture, strain localization mechanisms and deformation history. Earth and Planetary Sci. Lett., 407,
691   205-220.

692   Ulven, O. I., Beinlich, A., Hövelmann, J., Austrheim, H. & Jamtveit, B., 2017. Subarctic physicochemical
693   weathering of serpentinized peridotite. Earth Planet. Sci. Lett. 468, 11–26.

694   van der Straaten, F., Schenk, V., John, T. & Gao, J., 2008. Blueschist-facies rehydration of eclogites (Tian Shan,
695   NW-China): Implications for fluid-rock interaction in the subduction channel. Chem. Geol. 255, 195–219.

696   Van Goethem, L., Van Landuyt, J., & Amelinckx, S., 1978. Study of the glide elements in pyrite by means of
697   electron microscopy and electron diffraction. American Mineralogist, 63(5-6), 548-550.

698   Velásquez, G., Salvi, S., Siebenaller, L., Béziat, D., & Carrizo, D., 2018. Control of Shear-Zone-Induced

699 Pressure Fluctuations on Gold Endowment: The Giant El Callao District, Guiana Shield,
700 Venezuela. Minerals, 8(10), 430.

701 Viola, G., Mattila, J., Zwingmann, H., Todd, A. and Raven, M., 2011. Structural and K / Ar Illite
702 Geochronological Constraints on the Brittle Deformation History of the Olkiluoto Region , Southwest Finland
703 Structural and K / Ar Illite Geochronological Constraints on the Brittle Deformation History of the Olkiluoto
704 Region.

705 Vukmanovic, Z., Reddy, S. M., Godel, B., Barnes, S. J., Fiorentini, M. L., Barnes, S. J., & Kilburn, M. R., 2014.
706 Relationship between microstructures and grain-scale trace element distribution in komatiite-hosted magmatic
707 sulphide ores. Lithos, 184, 42-61.

708 Wang, H. A., Grolimund, D., Giesen, C., Borca, C. N., Shaw-Stewart, J. R., Bodenmiller, B., & Günther, D.,
709 2013. Fast chemical imaging at high spatial resolution by laser ablation inductively coupled plasma mass
710 spectrometry. Anal. Chem. 85, 10107–10116.

711 Williams, J. N., Toy, V. G., Smith, S. A., & Boulton, C., 2017. Fracturing, fluid-rock interaction and
712 mineralisation during the seismic cycle along the Alpine Fault. Journal of Structural Geology, 103, 151-166.

713 Wintsch, R. P., Christoffersen, R., & Kronenberg, A. K., 1995. Fluid-rock reaction weakening of fault
714 zones. Journal of Geophysical Research: Solid Earth, 100(B7), 13021-13032.

715 Zhang, Y., Cai, Y., Qu, Y., Wang, Q., Gu, L., & Li, G., 2020. Two-stage fluid pathways generated by volume
716 expansion reactions: insights from the replacement of pyrite by chalcopyrite. Scientific reports, 10(1), 1-11.

717 Zhao, J., Brugger, J., Chen, G., Ngothai, Y. & Pring, A., 2014. Experimental study of the formation of
718 chalcopyrite and bornite via the sulfidation of hematite: Mineral replacements with a large volume increase.
719 Am. Mineral. 99, 343–354.

720

Highlights

- Combined geochemical and microstructural study by LA-ICP-TOFMS and EBS analyses on sulphides
- Deformation-induced trace element mobility in natural sulphides under low-temperature and high fluid pressure conditions
- Sb, Ag and Sn as most effective tracers of intragranular deformation

Declaration of competing interest

The authors declare that they have no known competing financial interests or personal relationships

that could have appeared to influence the work reported in this paper.

Author statement

BM, GV and LM, conceived the paper. BM collected and processed laboratory data, provided their interpretations, drew the figures and wrote the paper. JM and GV sampled the outcrop and contributed to the interpretation of field data. BM, GS, CN, PKS, PSG, BH and DG acquired, processed and interpreted the LA-ICP-TOFMS data. BM and LM acquired and processed the EBSD maps. All author actively participated in discussing the results, drawing the conclusions, and manuscript revisions.
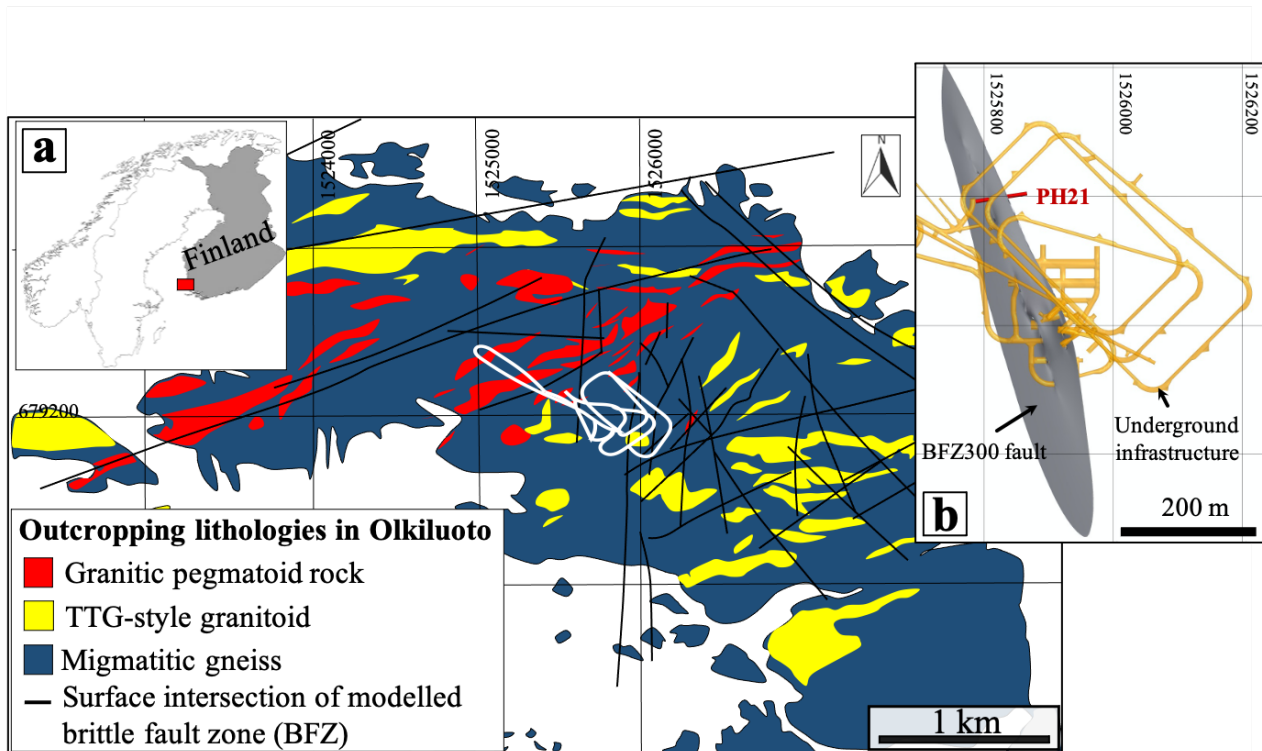
Figure 1. (a) Geological sketch of the Olkiluoto Island (SW Finland) and structural map, showing the surface intersection of modelled brittle fault zones (BFZ, modified from Aaltonen et al., 2016). Surface projection of the underground investigation facility is in white. Coordinates are given in the local KKJ1 coordinate system. (b) Modelled 3D surface of BFZ300 fault plane (grey) intercepted at ca. -421 m b.s.l. by the drill core PH21. Existing underground infrastructure is in yellow.
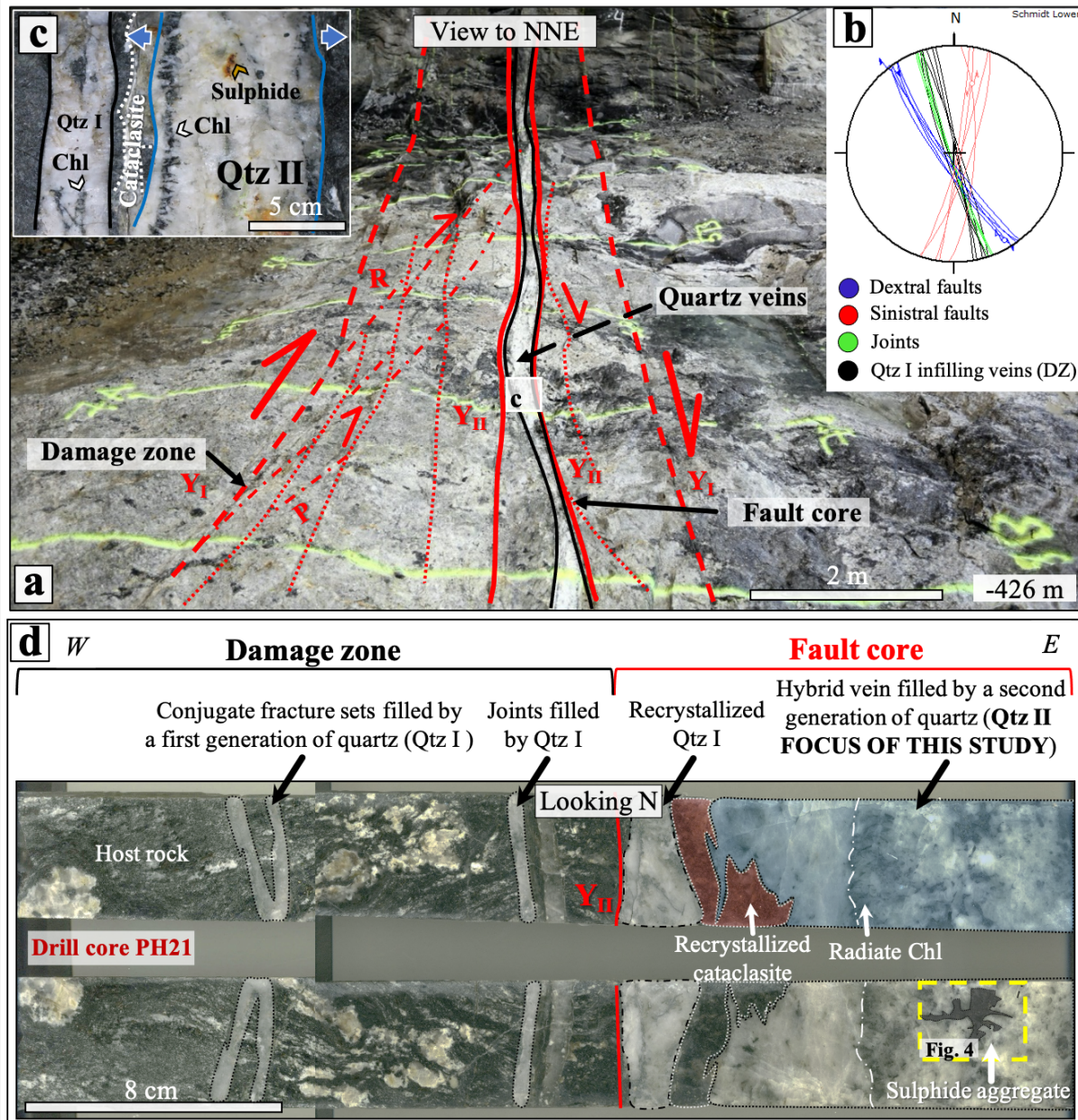
Figure 2. BFZ300 fault architecture. (a) The internal principal slip zone (Y_{II}) separates the damage zone from the fault core. (b) Lower-hemisphere, equiangular projection shows the structures in the damage zone. The damage zone is characterized by conjugate sets of fractures and joints infilled by a first generation of quartz (Qtz I), and barren fractures (joints). (c) Fault core is characterized by recrystallized Qtz I and by a younger generation of quartz-sulphides-chlorite bearing vein (Qtz II). The blue arrows indicate the vein opening direction. Modified from Marchesini et al. (2019). (d) PH21 drill core and structural interpretation. Yellow dashed line indicates the location of thin section PH21-3. PH21 was drilled horizontally with a trend of 080°. It intercepts BFZ300 at ca. -421 m b.s.l.
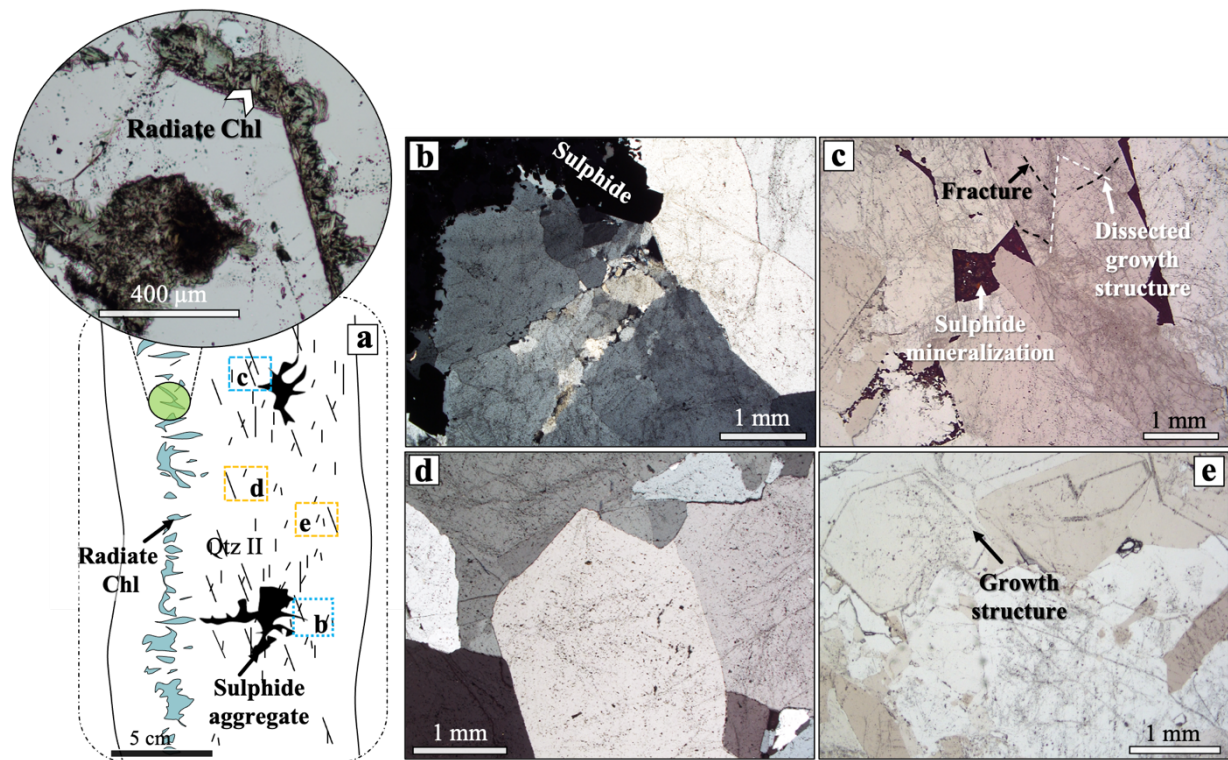
Figure 3. (a) Schematic fabric of the Qtz II vein. Inset shows textural equilibrium between quartz and chlorite. Host quartz is less deformed away from sulphide aggregates. (b) Close to sulphide aggregates, host quartz exhibits plastic distortion (undulose extinction) and it is (c) pervasively fractured by dense and pervasive network of intergranular and transgranular fractures (dashed black lines) dissecting primary growth structures (dashed white lines). (d) In the central part of the vein, at 4-5 cm from the sulphides, Qtz II crystals exhibit a lower degree of fracturing (only intragranular fractures) and no evidence of crystal plasticity. (e) Primary growth structures are well preserved.
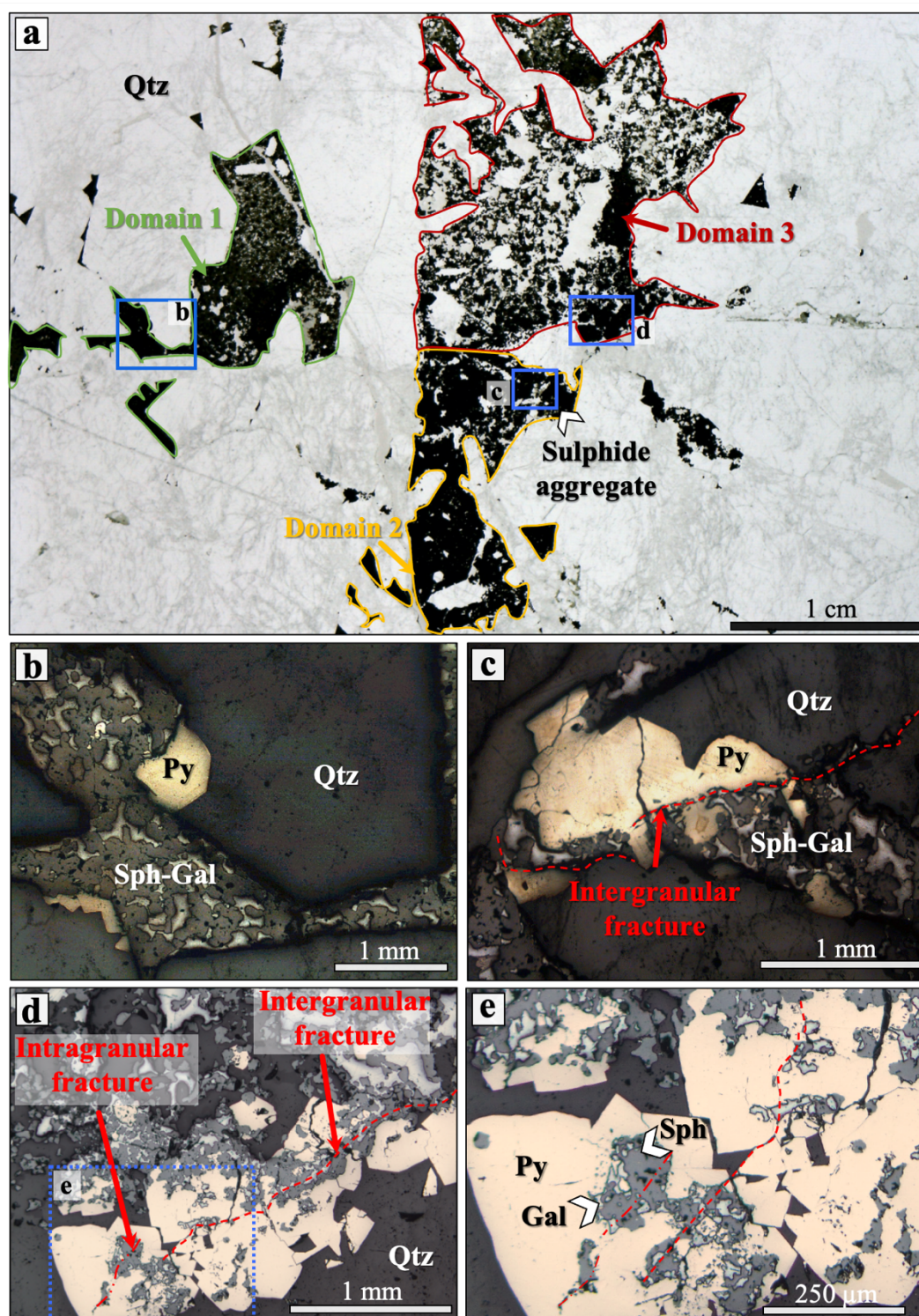
Figure 4. (a) Photomicrograph (plane polarized light) of a representative sulphide aggregate. The host quartz close to sulphide aggregate is highly fractured. Fractures are marked by trails of fluid inclusions. Three different structural domains were identified based on brittle deformation of pyrite and replacement of sphalerite and galena at the expenses of pyrite. (b) In Domain 1, pyrite exhibits a general euhedral texture, with minor anhedral sphalerite and galena deposited at the edge of the pyrite crystal. (c) In Domain 2 pyrite shows a subhedral texture. Replacement of pyrite by sphalerite and galena is locally observed along the pyrite crystal boundaries following the position of thin brittle intergranular fractures. (d) In Domain 3 pyrite displays a fractured texture and extensive replacement by sphalerite and galena along

discrete fractures. (e) Blown-up view of the replacement of pyrite into sphalerite and galena close to intragrain fractures and along crystal edges. Py: pyrite; Gal: galena; Sph: sphalerite; Chl: chlorite.
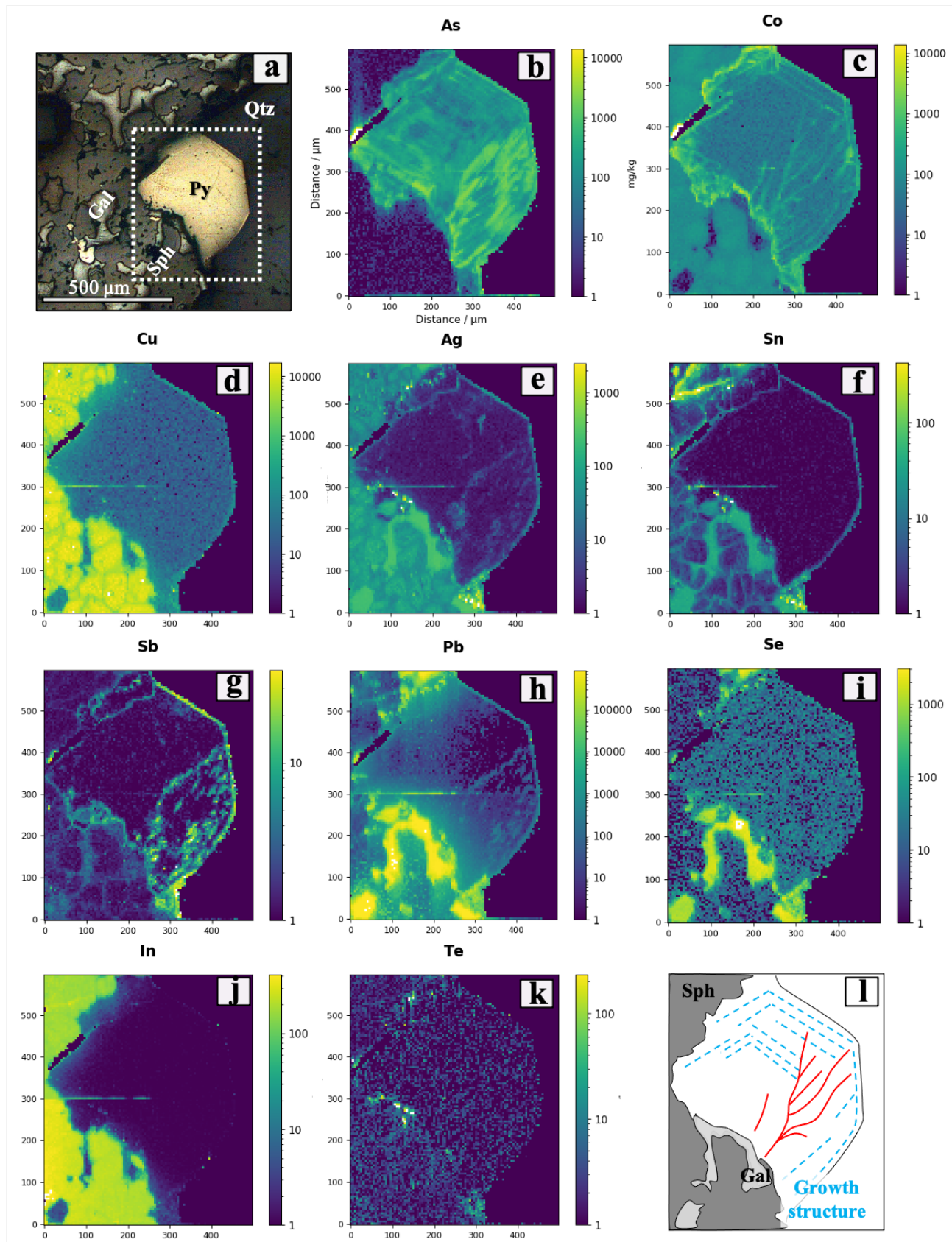
Figure 5. LA-ICP-TOFMS element distribution maps of sulphides in Domain 1. All panels show the same 500 x 600 μm sample area. All the color-coded vertical bars show the range of mass fractions of the indicated elements. (a) Reflected light photomicrograph of the analysed area, where the white dashed line defines the area analysed by LA-ICP-TOFMS. (b-k) Details on element distribution maps As, Co, Cu, Ag, Sn, Sb, Pb, Se, In, Te are given in the main text. (l) Synthesis

of the textural relationships between primary grow structures and the network of chemical structures identified in pyrite. The line with high concentration at 300 μm in the Y-axis is an artifact caused by the acquisition of the maps in sections. This artifact is located at the edge of the maps. Red lines indicate intragranular "chemical structures". Qtz: quartz; Py: pyrite; Sph-Gal: sphalerite-galena.
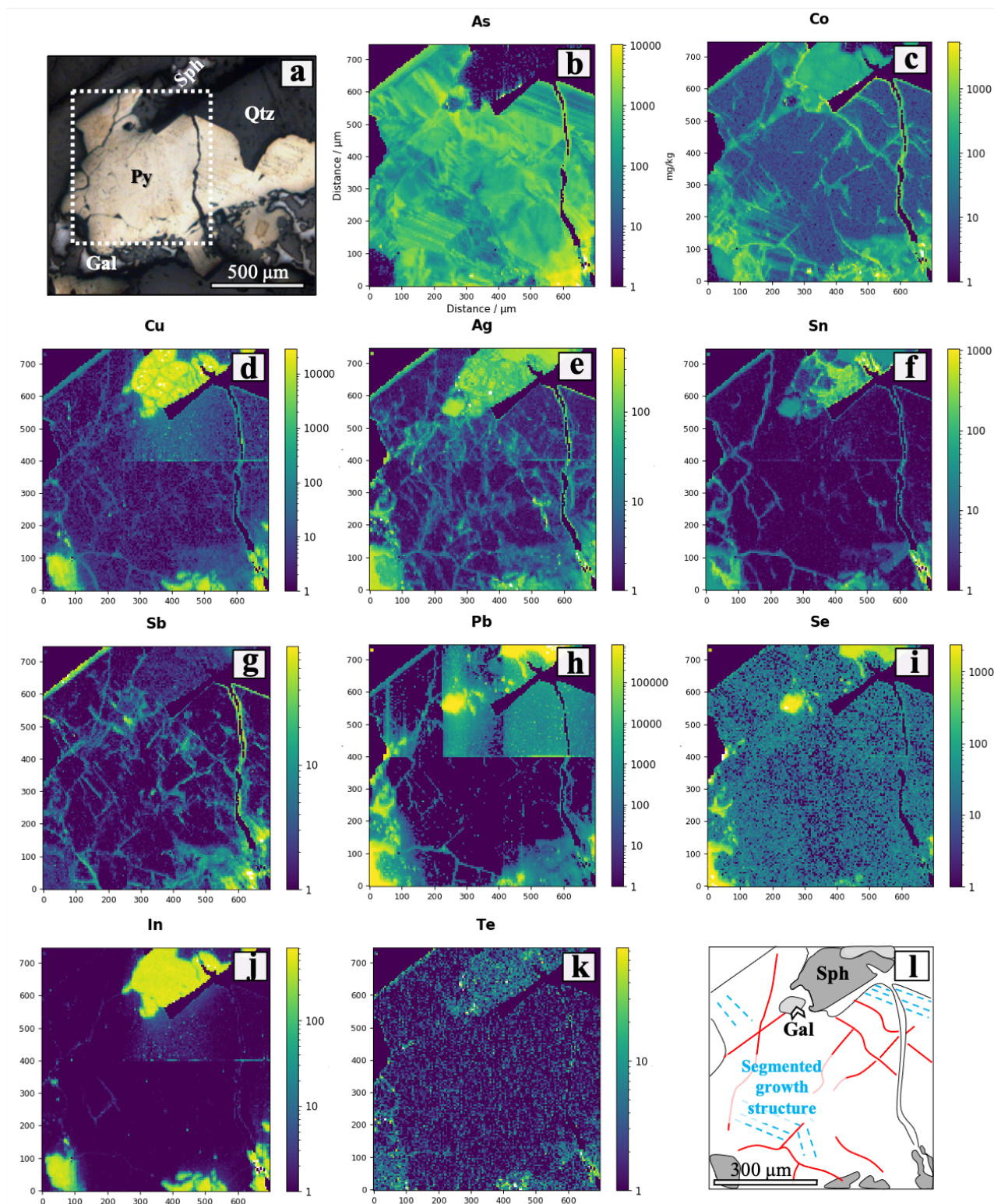
Figure 6. LA-ICP-TOFMS maps of sulphides in Domain 2. All panels show the same 700 x 700 μm sample area. All the color-coded vertical bars show the range of mass fractions of the indicated elements. (a) Reflected light photomicrograph of the analysed area. The dashed white line defines the area analysed with LA-ICP-TOFMS. (b-k) Distribution maps of As, Co, Cu, Ag, Sn, Sb, Pb, Se, In and Te show intragranular chemical patterns. Details are given in the main text. (l) Synthesis of the textural relationships between primary grow structures and the network of chemical structures identified in pyrite. The line with high concentration at 400 μm in the Y-axis is an artifact caused by the acquisition of the maps in sections. Red lines indicate intragranular "chemical structures". Qtz: quartz; Py: pyrite; Sph-Gal: sphalerite-galena.
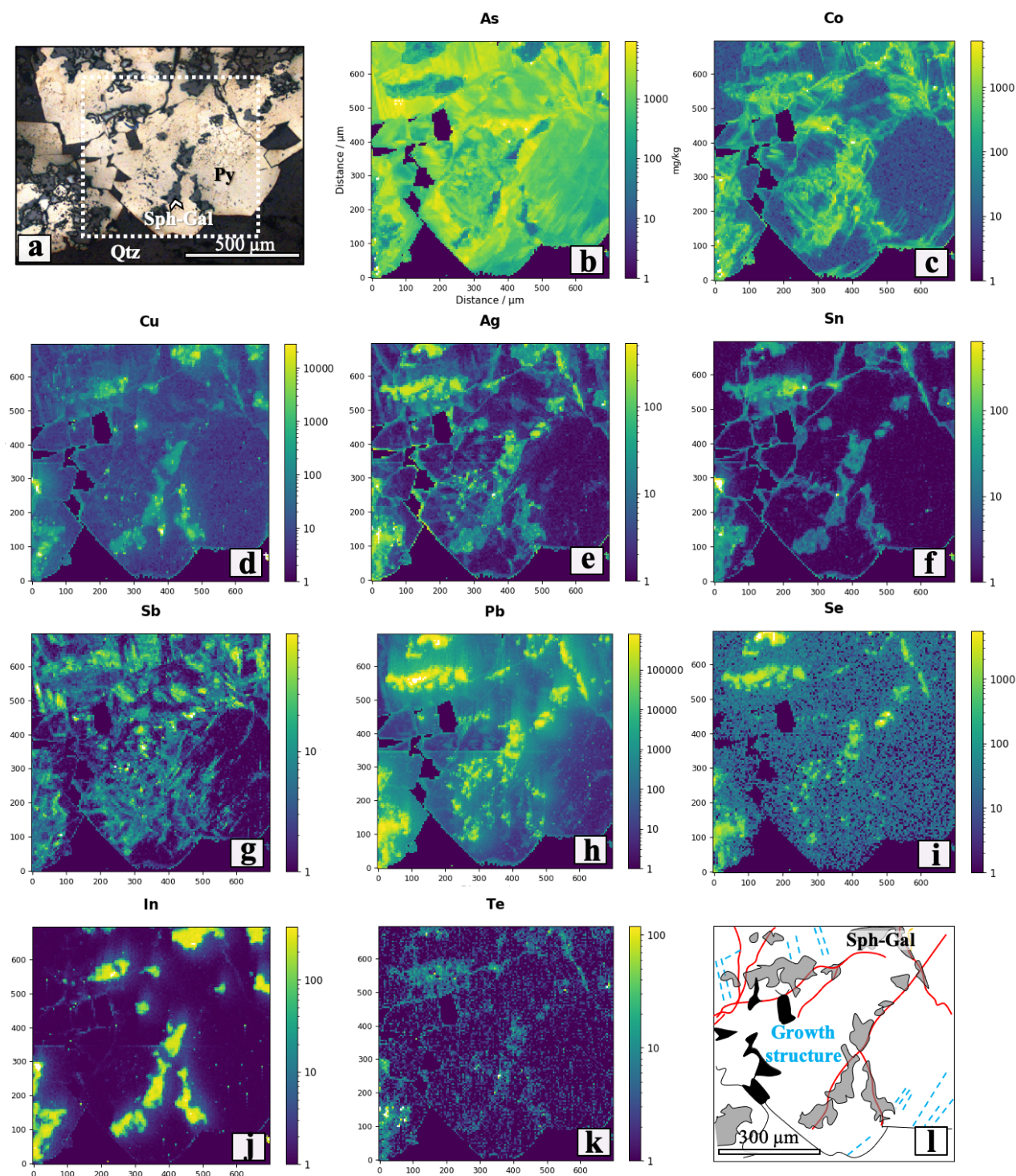
Figure 7. LA-ICP-TOFMS maps of sulphides in Domain 3. (a) Reflected light photomicrograph of the analysed area. The dashed white line highlights the analysed area. All panels show the same 700 x 700 μm sample area. All the color-coded vertical bars show the range of mass fractions of the indicated elements. (b-k) Details on element distribution mas of As, Co, Cu, Ag, Sn, Sb, Pb, Se, In and Te are given in the main text (l) Synthesis of the textural relationships between primary grow structures and the network of chemical structures identified in pyrite. Red lines indicate intragranular "chemical structures". Qtz: quartz; Py: pyrite; Sph-Gal: sphalerite-galena.

Figure 8. (a) Dashed white box indicates the analysed area with EBSD of a representative pyrite in Domain 2. (b) EBSD orientation map of pyrite, colour-coded according to the inverse pole figure (IPF) with respect to the X-direction (see text for explanation). IPF reference map is shown at the bottom right side. Low-angle (1.5-10°) boundaries are marked with a white continuous line, while grain boundaries (>10º) are shown in black. Grey pixels are non-indexed points. (c) Local misorientation (LM) map, colour coded according to the degrees of misorientation between each pixel and its neighbouring clusters of pixels within an area of 7x7 pixels. Colour scale is shown at the bottom right side. (d) Texture component (TC) map of Grain 1. The map is colour-shaded according to the angular misorientation from the reference point that is marked with a white cross. Trace of misorientation profile a-b oriented perpendicular to the low-angle boundary is shown in black. White dashed rectangle encompasses the sampled area for boundary trace analysis shown in (h). (e) Misorientation profile across the low-angle boundary in Grain 1 (a-b) shows a continuous increase in misorientation up to 4°. (f) TC map of Grain 3 and trace of misorientation profile c-d perpendicular to a representative section of the low-angle boundary. (g) Misorientation profile across the low-grain boundary shows a sharp step at 60 µm.

(h) Upper hemisphere, equal angle stereographic projection of the sampled dataset and boundary trace analysis. Our interpretation of the most feasible solution of the boundary trace analysis is sketched.
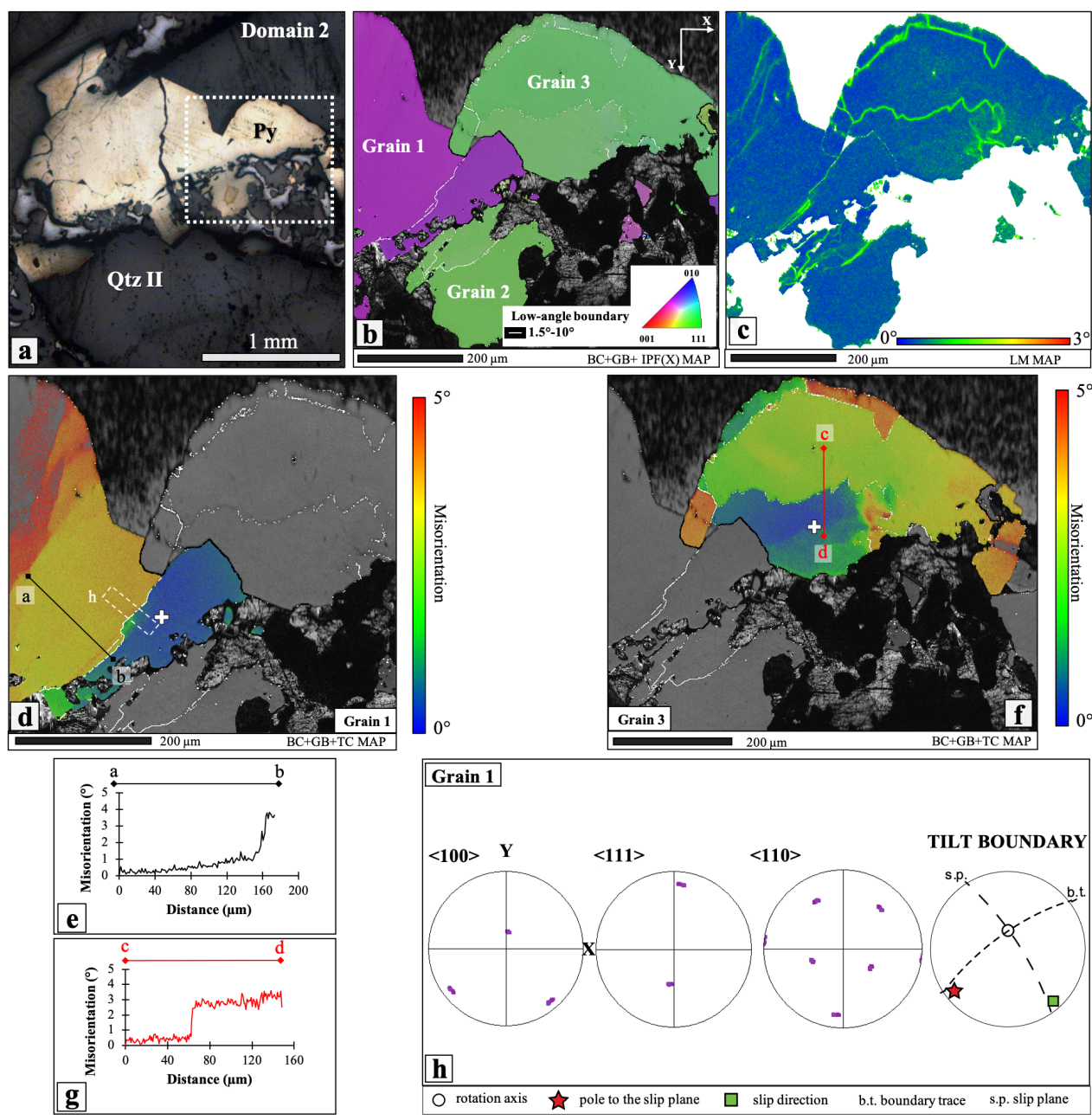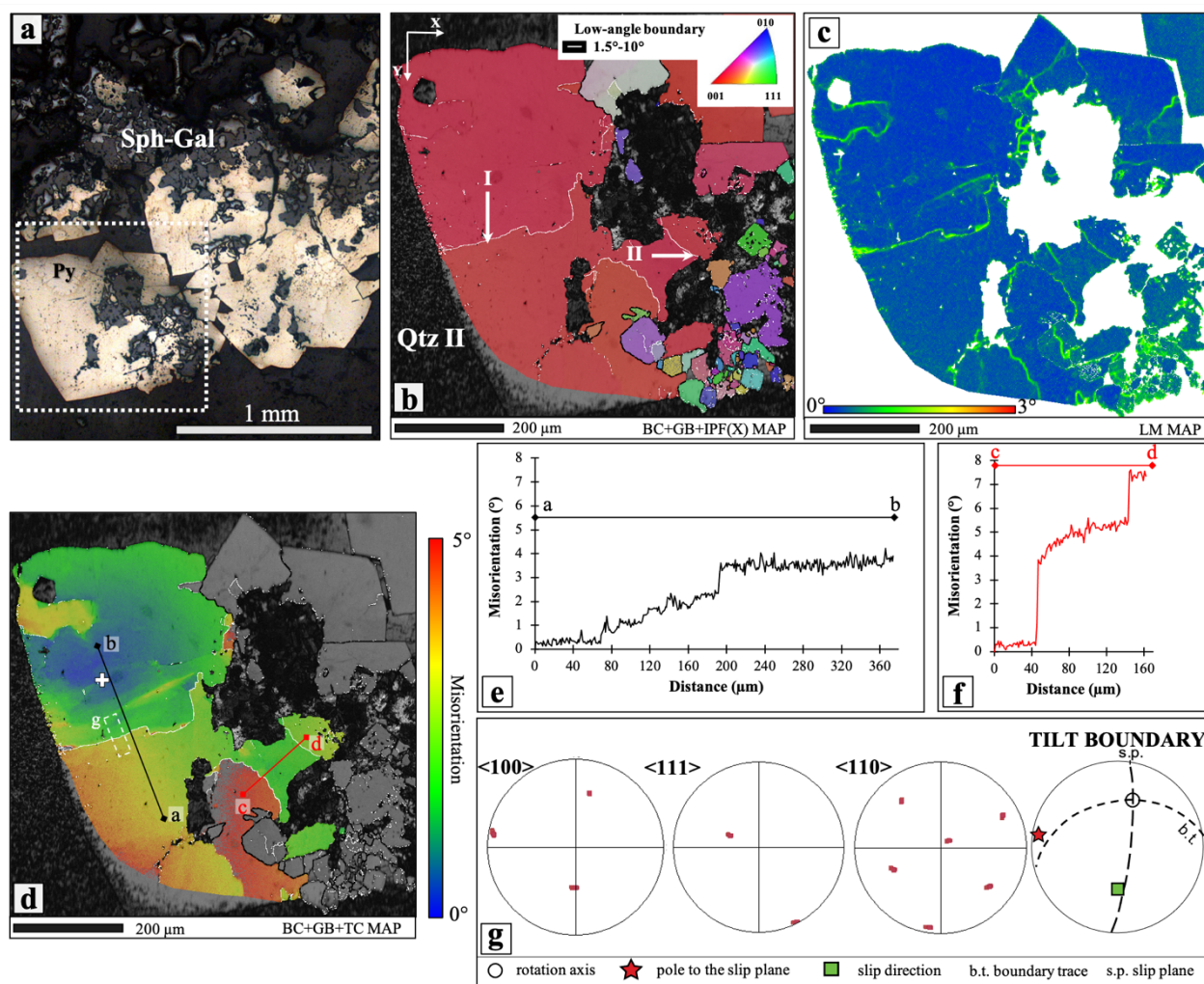
Figure 9. (a) Dashed white box indicates the analysed area with EBSD of a representative pyrite in Domain 3. (b) EBSD orientation map of pyrite, colour-coded according to the inverse pole figure (IPF) with respect to the X-direction (see text for explanation). Low-angle (1.5-10°) boundaries are marked with a white continuous line, whereas grain boundaries >10° are in black. Grey pixels are non-indexed points. (c) LM map, colour coded according to the degrees of misorientation between each pixel and its neighbouring clusters of pixels within an area of 7x7 pixels. Colour scale is shown at the bottom right side. (d) TC map highlights the spatial distribution of misorientation across the analysed area. The map is colour-shaded according to the angular misorientation from the reference point marked with a white cross. White dashed rectangle encompasses the sampled area for boundary trace analysis. (e-f) Misorientation profiles across the two distinct sets of low-angle boundaries. (g) Upper hemisphere, equal angle stereographic projection of the sampled dataset and boundary trace analysis. Our interpretation of the most feasible solution of the boundary trace analysis is sketched.

Figure 10. Conceptual model of fracturing and alteration of pyrite. (a) Pyrite (Py) precipitates in equilibrium with quartz (Qtz) and radiate chlorite (Chl) from a first batch of fluid. Sphalerite-galena-chalcopyrite assemblages precipitated as new phases from a later batch of fluids, enriched in Co, Cu, Ag, Sn, Sb, Pb, Se, In, Te. The new assemblages are arranged along intra- and intergranular fractures and they locally alter pyrite. The competence contrast between soft pyrite inclusions and harder host quartz may have enhanced local fracturing by stress concentration at the reaction fronts. This, in turn, may have favored the following percolation of Co, Cu, Ag, Sn, Sb, Pb, Se, In, Te-bearing fluid. Outside the reaction fronts the host quartz is less fractured. (b) Precipitation of sphalerite-galena-chalcopyrite assemblages along major fractures induce local microfracturing of pyrite, promoting fracture propagation and further alteration at the crack tips. Microcracks may thus locally exploit tilt boundaries and dislocations. Chemical alteration and trace element mobility in the system is also favored by the simultaneous activity of pipe and DIP diffusion along dislocations and tilt boundaries and volume change chemical interactions.